Materials Research Express

**PAPER**

# Design and performance of an ultra-flexible solid state supercapacitor based on thermo-crosslinking carbon nanotube paper/$Co_3O_4$ nanowire electrode

To cite this article: Hetao Chu *et al* 2019 *Mater. Res. Express* **6** 085628

View the article online for updates and enhancements.

IOP ebooks™

Bringing you innovative digital publishing with leading voices to create your essential collection of books in STEM research.

Start exploring the collection - download the first chapter of every title for free.

This content was downloaded from IP address 219.217.231.135 on 13/06/2019 at 08:03

**IOP** Publishing *Mater. Res. Express* **6** (2019) 085628 https://doi.org/10.1088/2053-1591/ab26e7

Materials Research Express

**RECEIVED**
23 April 2019

**REVISED**
23 May 2019

**ACCEPTED FOR PUBLICATION**
4 June 2019

**PUBLISHED**
12 June 2019

**PAPER**

# Design and performance of an ultra-flexible solid state supercapacitor based on thermo-crosslinking carbon nanotube paper/$Co_3O_4$ nanowire electrode

**Hetao Chu[1], Zhichun Zhang[1], Qianshan Xia[1], Yanju Liu[2] and Jinsong Leng[1]**

[1] National Key Laboratory of Science and Technology on Advanced Composites in Special Environments, Harbin Institute of Technology (HIT), Harbin, People's Republic of China

[2] Department of Aerospace Science and Mechanics, Harbin Institute of Technology (HIT), Harbin, People's Republic of China

**E-mail:** lengjs@hit.edu.cn

**Keywords:** carbon nanotube paper, supercapacitor, ultra-flexible electrode

Supplementary material for this article is available online

## Abstract

An ultra-flexible carbon nanotube paper (CNP) was achieved by thermo-crosslinking reaction between carbon nanotubes via high temperature annealing to enhance mechanical property, which was indicated from the tensile test, Raman spectra and conductivity measurement. Based on the mechanical enhanced CNP, a sandwich structure binder free, separator free and encapsulation layer free flexible solid state CNP/$Co_3O_4$ nanowire supercapacitor was proposed that could be executed in various external mechanical conditions. The high specific capacitance of device was 345.8 F $g^{-1}$, when current density was 0.15 A $g^{-1}$, and its good cycling stability after 5000 cycles kept about 75.9% of the initial capacitance. For various external mechanical conditions, such as bending, pressing, folding and tearing, the capacitance retention is 74.9%–81.3%. Proof-of-concept of the multi-shape survived supercapacitor presents a strategy for designing a novel electrochemical device that could resist harsh external mechanical conditions in future application fields required the safety of a power supply system.

## 1. Introduction

Flexible, portable and wearable devices rapid growth triggers the increasing demand for transformable high energy storage resources [1–3]. Flexible all solid state supercapacitor is a forefront energy storage technologies, especially in the field of highly integrated equipment and portable devices [4] where require light weight [5, 6], multi-shapes [7–9], compressible and anti-failure to provide roll-up displays [10], bendable mobile electronic products and embedded monitoring devices. Moreover, wearable and high stretchable [11–13] wire-like supercapacitors are gained wide attention because the flexibility and stitchability provide giant potential applicaion in daily life. However, current research on supercapacitors has concerned on bulk electrodes and separators and the devices are too ungainly to apply for flexible energy storage carrier. Moreover, for the traditional supercapacitors, it is hard to survive once the devices are damaged by external force, which is not desired in practical application, such as supercapacitor dependent vehicles or aircraft. It is terrible if power supply system shut down immediately when supercapacitors are weakly damaged in external force. Therefore, it is necessary to provide a supercapacitor that could resist harsh external mechanical conditions. In that case, once devices are damaged, the excellent retention capacitance could offer maintenance time for a power supply system. Accordingly, achieving innovative supercapacitor with superior flexibility that enables to work well in bending, pressing, folding and tear shapes is still a challenge, due to the weak flexibility of electrode. Significant effort has been aroused to realize these problems such as various transition metal oxides or conductive polymer have been integrated with soft materials as electrodes for flexible hybrid supercapacitors (HSs) [14–17].

© 2019 IOP Publishing Ltd

However, hybrid electrodes consisting of conductive polymers or transition metal oxides possess low electric conductivity often decreases the electrochemical performance [15]. In addition, conductive polymers also have been involved in diverse carbon materials (graphene, carbon nanotubes or carbon fibers) [18] as electrodes for flexible electrodes. Nevertheless, conductive polymer is typically introduced by electrodepositing [19–21], which decreases the flexibility and conductivity of the initial carbon materials inevitably. Therefore, fabrication of ultra-flexible supercapacitor electrodes is a required technology for future novel energy device.

As a type of flexible energy storage devices, films like solid state supercapacitors get great attention in the past several years [14, 22, 23]. Compared with the traditional liquid electrolyte supercapacitors, freestanding film electrodes simplify supercapacitor packing by removing inactive components such as binders and current collectors, and enhance the energy density in view of the total device weight, which provides a promising strategy for developing lightweight and flexible supercapacitors. However, most of the reported conductive carbon film electrode requires integrating with polymer substrate such as polyethylene terephthalate [24, 25] or polyimide [26, 27] as a protection encapsulation layer to achieve moderate deformation, because most of the carbon films are fabricated from CNTs or graphene precursor by Van der Waals force possessing weak mechanical property that is unable to meet complicated deformation. Carbon nanotube paper (CNP), 2D geometric materials possess numerous advanced properties, is supposed to one of the suitable candidates to present pretty flexible electrodes. Currently, flexible electrodes of supercapacitors are mainly prepared with carbon black [22], free standing carbon nanotube films [28], reduced graphene oxide [29, 30] or carbon cloth [31, 32]. Additionally, to enhance the electrochemical performance, numerous works have paid attentions to the combination of carbon materials with high faradic pseudocapacitances transition metal oxide, such as NiO [33], $TiO_2$ [34, 35], $V_2O_5$ [36], and $MnO_2$ [37, 38], to enhance the specific capacitance. However, nanoscale transition metal oxide crystals interrupt the Van der Waals force interaction of CNTs or graphene resulting in poor flexibility electrodes that is hard to deform in complicated shapes, which is a grave drawback for flexible supercapacitor. In addition, based on the literatures [39–41], CNP prepared by infiltrating CNT suspension has weak mechanical property and flexibility [42, 43], which is hard to achieve multi-shapes for ultra-flexible supercapacitor electrode, such as pressing, small radius of curvature bending and folding conditions. Therefore, it is necessary to enhance mechanical properties of the CNP for ultra-flexible supercapacitor electrode.

In this paper, we report a mechanical enhancement CNP via high temperature annealing strategy to increase flexibility of the as-prepared CNP. From the characterizations of mechanics, Raman and conductivity, high temperature annealing process causes thermo-crosslinking reaction between CNTs. Based on the mechanical enhanced CNP, an ultra-flexible solid state symmetric supercapacitor, that is capable of bending, pressing, folding and even tearing, was constructed in a facile approach in a sandwich structure CNP/$Co_3O_4$(PVA gel)/CNP. The reported supercapacitor could keep a high performance specific capacitance in various external mechanical conditions, which provide maintenance time once the device is broke by external force in future supercapacitor dependent application field. In addition, to lose total weight of the device, the sandwich structure supercapacitor is binder-free, separator free and encapsulation layer free to increase the device energy density. In this case, the device thickness is much thinner than traditional liquid electrolyte supercapacitors and provides high flexibility. Above all, based on the thermo-crosslinking CNP, we propose a proof-of-concept flexible supercapacitor for resisting harsh external mechanical conditions in future application fields required the safety of a power supply system.

## 2. Experimental

### 2.1. Preparation of as-prepared CNP and annealing CNP

The as-prepared CNPs were fabricated by using a method reported previously [44, 45]. Typically, 0.5 g single wall carbon nanotubes (SWCNTs) was combined with 2.5 g Triton X-100 and dispersed by shear disperser (DS 50, EXAKT) for three times forming a paste-like carbon nanotube. The shear dispersion process could make the Trition coated on the carbon nanotubes of carbon nanotube bundles evenly. Subsequently, the pasty mixture was placed in a beaker and diluted by 5 L deionized water and the suspension was dispersed dynamically by an ultrasonic processor. Then the suspension was available through a filter membrane to form a carbon film. After drying 1 h at 100 °C, peeled off the CNPs were from the porous membrane. The thickness could be controlled by the CNT suspension concentration. The CNPs thickness, in this work, is about $\sim$30 $\mu$m (surface density $\sim$2.1 mg $cm^{-2}$) as shown in table S1, which demonstrates a pretty lightweight structure compared with the previous reports and provides a flexible substrate [42, 43]. To increase the CNP surface area, the surfactant was introduced as a sacrificial coating that not only increases the dispersibility but also serve to the porosity after pyrolysis at 380 °C. To obtain the annealing CNP, the above CNP after heat treatment was operated in a tube furnace at 1500 °C for 2 h in argon atmosphere and then anneals to room temperature.

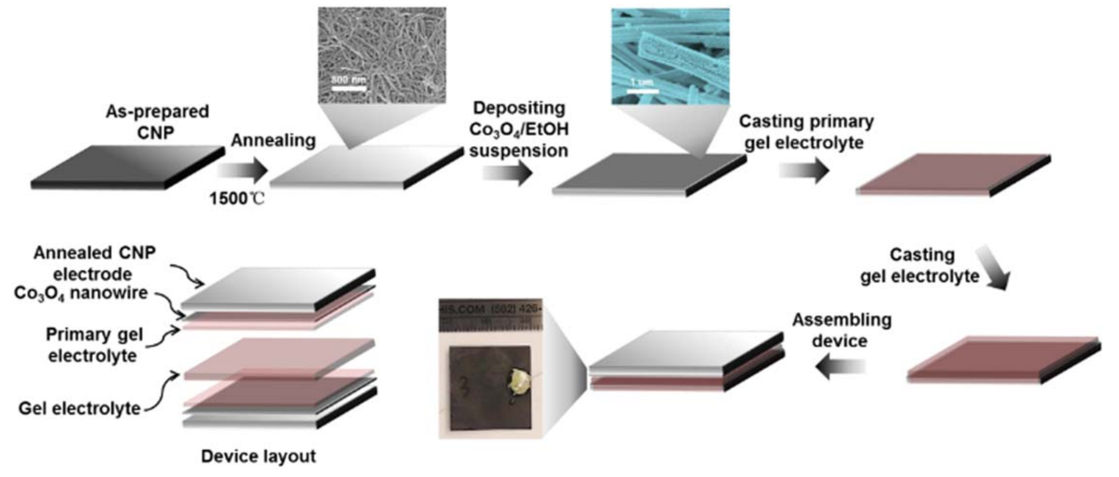

**Figure 1.** Schematic diagram of the preparation and assembly process for the flexible annealed CNP/$Co_3O_4$ nanowire supercapacitor and the side view layout shows the detailed layer of the composite device.

### 2.2. Synthesis of free $Co_3O_4$ nanowires

Urea (5 mmol) and $CoCl_2$ (5 mmol) were added into deionized water (15 ml), then the solution was stirred for 20 min. Next, the mixture solution was transferred to an autoclave of 30 ml volume. Subsequently, the hydrothermal autoclave was processed at 150 °C for 16 h. After cooling to room temperature, a light-pink precipitate was generated. The precipitate was washed by deionized water 3 times and dried in a vacuum oven at 50 °C for 1 h. To obtain the $Co_3O_4$ nanowires, heat the pink powder at 300 °C for 3 h. The as-prepared $Co_3O_4$ nanowire was dispersed in ethanol in an ultrasonic processor to form a suspension.

### 2.3. Preparation of solid electrolyte

3 g Polyvinyl Alcohol (PVA, Mw 140 000–180 000) was coupled with 30 ml deionized water at 80 °C using a stirring bar for 30 min until become a transparent solution in a 50 ml glass bottle. Then, 3.36 g (0.06 mol) KOH was placed on the transparent solution, and the mixture was stirred for 1.5 h at 80 °C continuously. After that, the gel electrolyte was cooling to room temperature and deposited on the electrodes and dried to obtain the solid electrolyte.

### 2.4. Fabrication of flexible HSs

The annealed CNPs were cut in pieces, 2.0 cm by 2.0 cm, and keep in ethanol before the device assembly. The CNPs mass loading was about 2 mg $cm^{-2}$ with surface area ~377 $m^2$ $g^{-1}$ as list in table S2, which is significantly higher than previous film like carbon material [31, 46]. $Co_3O_4$ nanowires suspension was prepared by dispersing 1.0 g $Co_3O_4$ in 20 ml ethanol. Then, the $Co_3O_4$ suspension was deposited on the flexible CNP substrates evenly using pipette as the ethanol evaporating by heating. After that, the PVA gel electrolyte was cast on the CNP/$Co_3O_4$ electrodes and dried for 30 min to evaporate most of the water contained in the electrolyte to fix $Co_3O_4$ nanowire on CNP surfaces. The fresh gel electrolyte was cast on both electrodes and assembled symmetric electrode (electrolyte side pressed face to face) solid state flexible HSs (measuring by multi-meter to resist short circuit). The schematic diagram and the device layout are given in figure 1.

### 2.5. Characterizations

Sample topography were observed using a scanning electron microscopy (SEM, Carl Zeiss) with an accelerating voltage of 10 kV and element distribution of samples was analyzed with energy dispersive x-ray spectroscopy (EDX). Moreover, Cross section view was undertaken by Focused Ion Beam (Helios NanoLab, FEI). The crystal characteristics of $Co_3O_4$ nanowires samples were identified through a x-ray diffractometer (Shimadzu XRD-6000) by a Cu k$\alpha$ source (scan step: 0.02°; scan range: between 10° to 75°). Raman spectra were carried out using Almega-Dispersive Raman (Thermo Nicolet). Atomic force microscope was observed by a Bruker Multimode 8. Transmission electron microscopy (TEM) images were performed with a high-resolution microscope (JEOL JEM-2010) at an accelerating voltage of 200 kV. Nitrogen adsorption isotherm measurement at 77 K was investigated utilizing a Micro metrics ASAP 2020 volumetric adsorption analyser. Mechanical property of composite was tested by Zwick/roll Materials Testing Machine (100 loading cell) with the testing method follows the specification of ASTM D638 Type VI. With a heating rate of 10 °C $min^{-1}$, thermal gravity analysis (TGA) in the inner atmosphere was encountered using a Mettler Toledo TGA/DSC1 instrument from room temperature to 1000 °C. Conductivity of sample was tested by a Napson Resistivity Measurement System (RG-7C) Four Point Probe.

### 2.6. Electrochemical performance measurements

Flexible HSs were tested in two electrode electrochemical cells using the KOH solid state electrolyte at room temperature. Two identical CNPs/$Co_3O_4$ hybrid electrodes were used in testing. According to the symmetric electrodes, the specific capacitance of the hybrid samples could be calculated from the charge-discharge curves utilizing the following equation [47]

$$C = (2I \times \Delta t)/(m \times \Delta V) \tag{1}$$

where C is the specific capacitance, I refers to the discharge current (A), Δt stands for the discharge time (s), m is the mass of electrode and ΔV refers to the potential change (V). The specific capacitance derived from CV curves could be derived from the following equation:

$$C = 2\left(\int I\, dV\right)/\Delta Vmv \tag{2}$$

where I indicates the voltammetric current, ΔV refers the applied potential in the sweep segment; m is the mass of the electrode; v is the potential scan rate.

All the charge-discharge, cyclic voltammetry (CV), and cycling measurements of the assembled HSs were tested by Gamry Reference 600 potentiostat (Gmery Instruments, Inc., USA). The potential window studied was between 0.8 V to −0.8 V. Electrochemical impedance spectroscopy (EIS) was employed a frequency range (from 100 to 0.01 kHz) and an AC amplitude of 5 mv at an open circuit potential.

## 3. Results and discussion

### 3.1. Morphology characterization of as-prepared and annealed CNP

The morphology of a large scale as-prepared CNP was demonstrated in figure 2(A) with the size of $370 \times 370 \times 0.030\ mm^3$. The dimension of the diagonal line is approximately 20 inches, which is suitable for general electronics such as diminutive flexible display, flexible HSs and wearable device substrates. Additionally, various sizes and shapes of as-prepared CNPs were able to fabricate by changing the filter substrate (figures S1(A)–(C)), performing the remarkable advantages of the CNT suspension infiltrated process for producing scalable CNPs. It is evident that CNPs are smooth and the wrinkles on the surface indicate the CNPs are extremely thin. Figure 2(B) is the SEM image of the CNP before high temperature annealing. Apparently, CNT bundles entangle together forming a random non-woven CNT network. Due to electrostatic force, large amounts physical crosslinking points are produced, which could afford for mechanical properties. In addition, the small amount amorphous particles and rough CNT bundles indicate the surfactant attached on CNT bundles or aggregated as particles resulting in decreasing CNT porosity and conductivity. In order to improve the as-prepared CNP mechanical property, conductivity and surface area, the as-prepared CNPs were heated at 380 °C in inert atmosphere (figure S2) for 2 h in a tube furnace to eliminate the surfactant and then were annealed at 1500 °C for 2 h to form thermo-crosslinking CNP. Figure 2(C) shows the CNPs after high temperature annealing. Obviously, a homogeneous CNP with a mass of physical crossing points is fabricated by self-assembly processing. According to the literatures [48–50], at high annealing temperature, carbon materials are able to generate thermo-crosslinking reaction between the defective atoms, which could increase the mechanical property of as-prepared CNP. The smooth CNT bundle surface and high porosity represents the residual surfactant was removed totally. It is noticeable the pore structure after annealing is much clear than that as-prepared CNP, because surfactant pyrolysis open the pores filled in the figure 2(B). The inserted CNPs folded by a tweezer presents the annealed CNP could be bended at a small radius of curvature, which shows the annealed CNPs possess high flexibility and excellent mechanical property. High flexibility ensures the annealed CNP/$Co_3O_4$ supercapacitor could be used in multi-shapes under external mechanical force, such as bending, pressing and folding conditions. To investigate the morphology change before and after annealing, cross sections of the CNP before and after annealing are manufactured by focused ion beam as shown in figure 2(D). The front view profile was dug by plasma bombardment and then polished under different plasma current to obtain clear topography. High magnification cross section morphologies of the CNP after thermolysis of dispersant at 380 °C and after annealing at 1500 °C are displayed in figures 2(E) and (F), respectively. It is obvious the as-prepared CNP is much more porous than annealed CNP. Based on the report [48], at high annealing temperature, part of the defective atoms could form the covalent bond between CNTs leading to the decrease of pore density, which indicates the thermo-crosslinking reaction should happen at high annealing temperature.

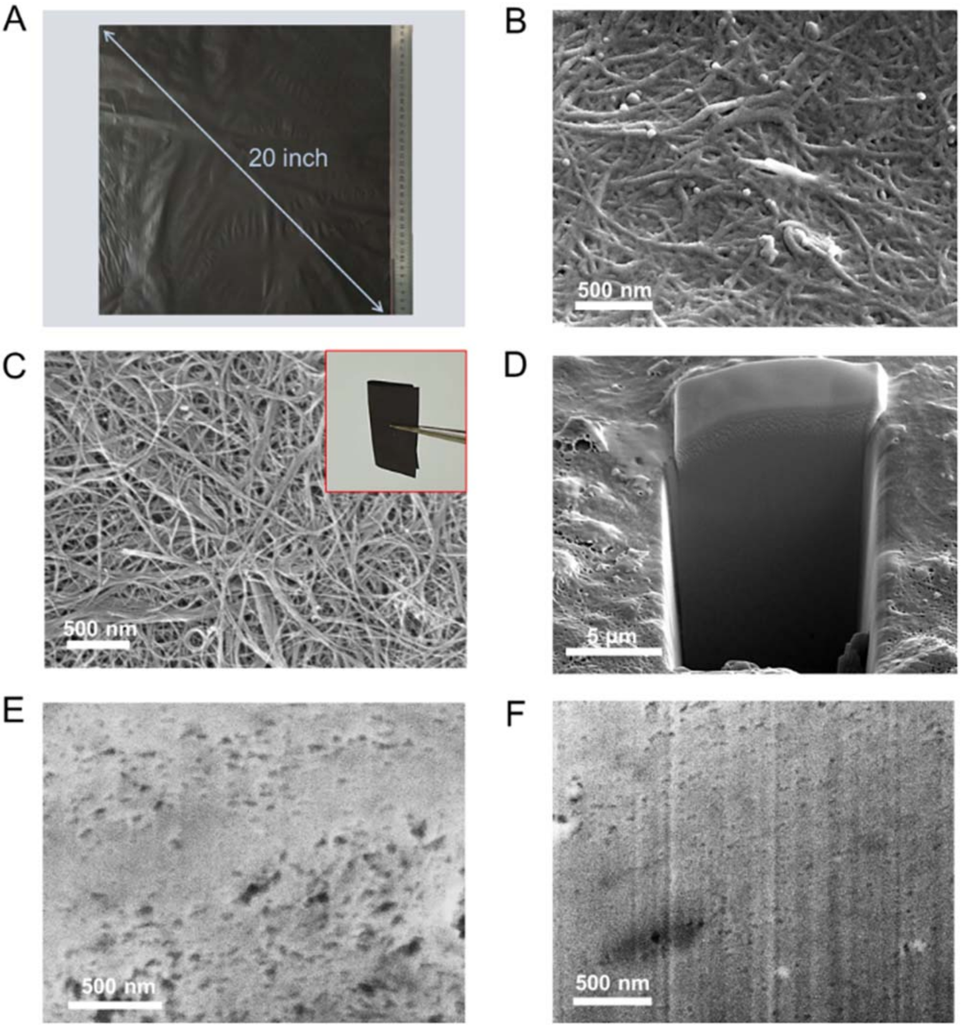

**Figure 2.** (A) A digital photo of as-prepared CNP before residual surfactant pyrolysis. (B) SEM image of the as-prepared CNP before the surfactant pyrolysis. (C) Surface morphology of the annealed CNP. The insert image is an annealed CNP folded by a tweezer at a small radius of curvature. (D) Front view profile of the cross section fabricated by focused ion beam. High magnification cross section SEM image of the (E) CNP after heat treatment at 380 °C; (F) CNP after annealing at 1500 °C.

### 3.2. Pore feature analysis

To display the pore feature of the CNP after heat treatment, its AFM image is presented in inset of figure 3(A). It is understandable the random CNT bundle is a porous film like the morphology shown in figure 2(C). The pore depth for the AFM image is declared in figure 3(A). Apparently, the porous depth conforms to Gaussian distribution with 80% percentages porous locating at 50–60 nm. Porous dimension of the annealed CNP is about 20 nm in width and 60 nm for depth. The pore structure of the as-prepared and annealed CNP was investigated by nitrogen adsorption isotherms at 77 K as shown in figure 3(B). Obviously, for the as-prepared sample, a weak porous feature was founded in the isotherms curve because of the overlap of the adsorption branch and desorption branch, which prove the surfactant filled pores. However, after annealing, a clear pore feature is demonstrated and the porous characteristic typically conformed to type IV isotherm with H1 hysteresis loop indicating the heated CNPs is an ordered mesoporous structure, which could enhance the Double-layer capacitance. Inserted curves are pore diameter distribution calculated by Barret-Joyner-Halenda (BJH). Compared with the as-prepared sample, the two peaks at 3 and 22.5 nm are produced after annealing treatment indicating the most pores in sample belong to the mesoporous structure. Surface area data calculated by different method of the as-prepared and annealed CNP is presented in table S2. It is quite clear that after annealing, surface area calculated by BET and Langmuir increase by 7.74 and 7.23 times, respectively. What's more, from the BJH adsorption/desorption cumulative surface area values, pore size between 1.7–300 nm, the surface area increases by 7.5 and 8.0 times, respectively. The two peaks at 3 nm and 22.5 nm and pore distribution between 1.7–300 nm show the annealing CNP is a hierarchical structure which is helpful for electrolyte ions injecting into electrodes.

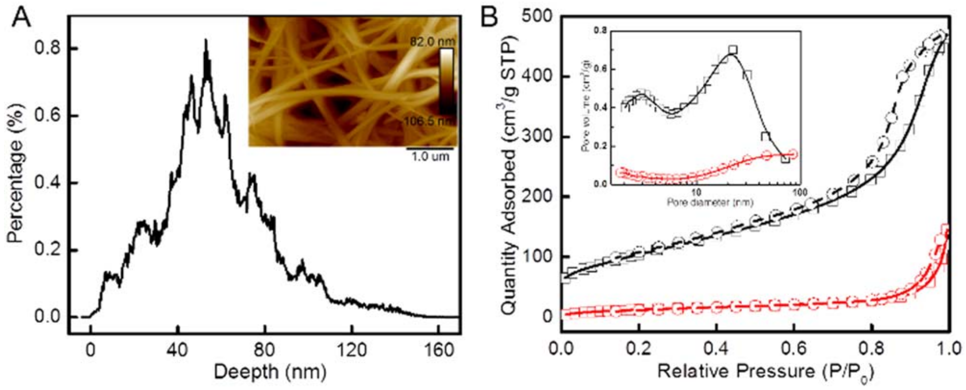

**Figure 3.** (A) Pore-depth distribution for the AFM phase image (inserted photo). (A) Nitrogen adsorption isotherms of the CNPs before heat treatment at 380 °C (Red curve) and after annealing at 1500 °C (Black curve). Inset is the pore-width distribution of the corresponding samples.

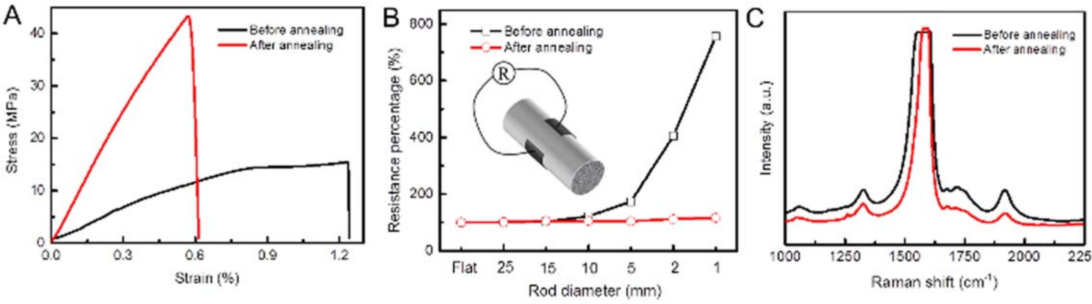

**Figure 4.** Characterizations of the CNP before and after annealing (A) tensile test; (B) flexibility test; (C) Raman spectra.

### 3.3. Feature analysis of the annealed CNP

To further investigated thermo-crosslinking effect, the CNP before and after annealing were characterized by tensile test, flexibility test and Raman spectra (figure 4). Figure 4(A) shows tensile stress and strain value of the annealed and control samples is 43 MPa, 0.56% and 15.4 MPa, 1.23%, respectively. It is can be concluded that the fracture strength after annealing was increased by 23 times higher than the previous report [1]. After annealing treatment, the tensile stress increases by 179% and the tensile strain decreases by 120%, which indicate thermo-crosslinking reaction happened at the high temperature. Due to thermo-crosslinking effect between CNTs, the sliding trend between CNTs is limited to increase the tensile stress and decrease the tensile strain, while the as-prepared CNPs only exist Van der Waals force to resist the tensile signifying a weak mechanical property. In addition, for the as-prepared CNP, the smaller slope of the terminal part declares the sliding behavior between CNTs. Figure 4(B) is the flexibility test of the as-prepared and annealing CNP. The resistance was measured by wrapping a piece of CNP on the rods with different diameter. The contact resistance between CNTs is change when the CNP was bended in a small radius of curvature. It is obvious that the resistance of as-prepared CNP increases sharply when the rod diameter from 10 mm to 1 mm. Resistance percentage at 1 mm rod diameter is 756% of the flat CNP, which generated a serious crack in small radius of curvature. However, for annealed CNP, the resistance has a slight change (increased by 17%) when the bending diameter decreases from 25 mm to 1 mm. Therefore, the tensile and flexibility tests reveal thermo-crosslinking happened at high annealing temperature. Raman spectra of the CNP before and after annealing were shown in figure 4(C). Peaks at 1325.5 cm$^{-1}$ and 1586.2 cm$^{-1}$ are attributed to D band and G band. Compare with as-prepared CNP, the strength ration $I_D/I_G$ of annealed CNP decreases from 0.2 to 0.12 indicating the defective atoms are decreased after the annealing. The peak D bond strength of as-prepared CNP shows a little defect exist in the initial CNTs. Therefore, the ratio ($I_D/I_G$) decreases of annealed CNP may be caused by thermo-crosslinking reaction. The shrink of G band width of the annealed CNP also demonstrates the increase of graphitization degree after annealing. The electric conductivity of the annealed CNP is about 380 ∼ 395 S cm$^{-1}$, which increases 1.41–1.55 times than the CNP treated at 380 °C (table S1). The conductivity increase proves the covalent bonds of C-C are formed during the thermo-crosslinking at high temperature.

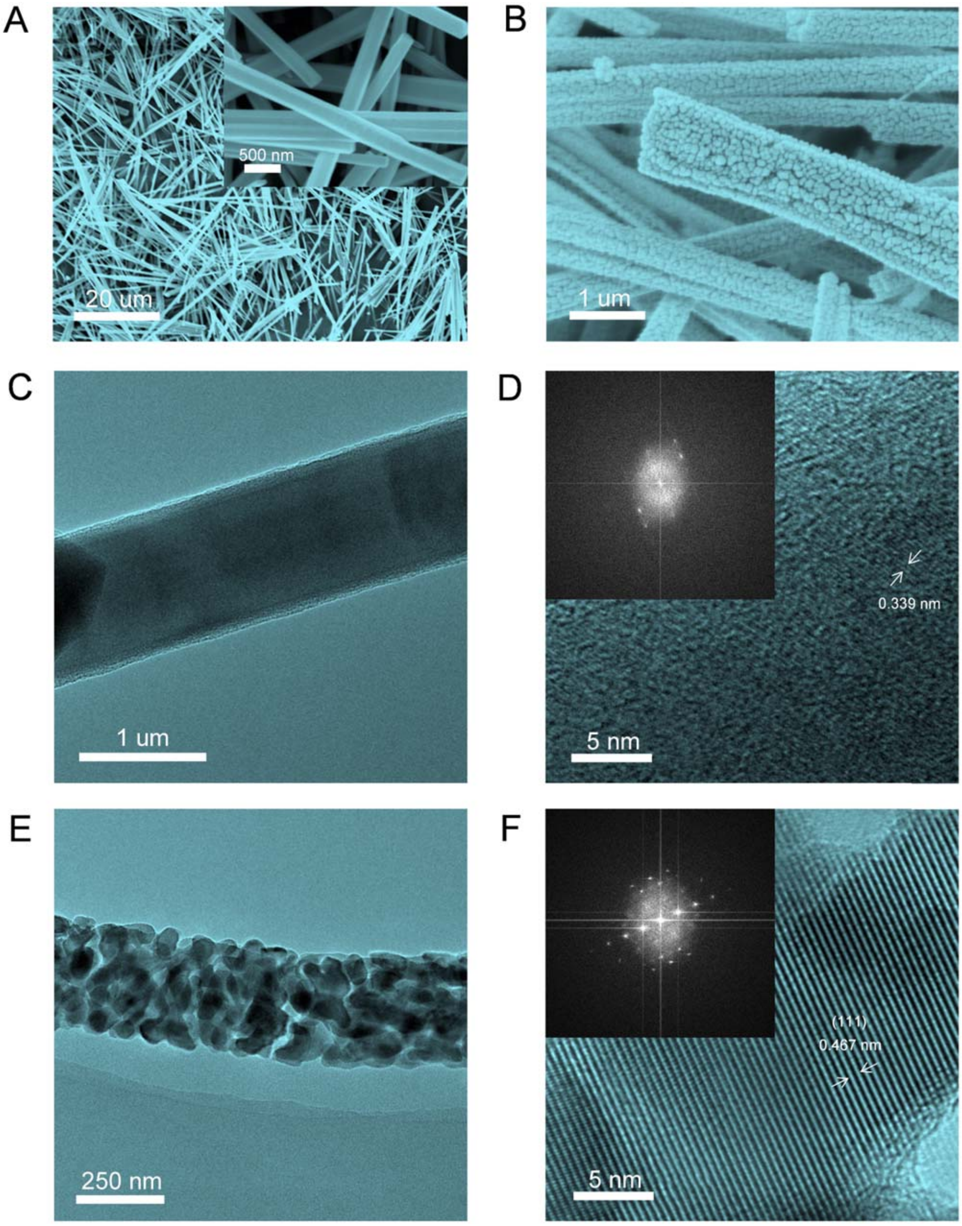

**Figure 5.** (A) The SEM image of $Co(OH)_2$ nanowires. Inset illustrates the high magnification morphology. (B) SEM image of $Co_3O_4$ nanowires. (C) TEM characterization of the $Co(OH)_2$. (D) HR-TEM image of $Co(OH)_2$. Inset draws crystal electron diffraction of the HR-TEM area. (E) TEM illustration of the $Co_3O_4$. (F) HR-TEM image of $Co_3O_4$. Inset draws crystal electron diffraction of the HR-TEM area.

### 3.4. Characterization of $Co_3O_4$ nanowires

The morphologies of the $Co(OH)_2$ and $Co_3O_4$ nanowires were characterized using SEM and HR-TEM, revealing that a uniform as-prepared nanowires (figure 5(A) and inset) were achieved by hydrothermal method with the diameter in the range of 500–700 nm and length of ~30 um. From the inset, $Co(OH)_2$ are well-crystalized nanowires with high purity. After sintering treatment, $Co(OH)_2$ nanowires transfer to $Co_3O_4$ nanowires which are proved in figure 5(B). It is apparent that the surface of the $Co_3O_4$ is much roughness than that before sintering treatment. The $Co_3O_4$ nanowires are composed of numerous nanoparticles maintaining a wire shape, due to generating water molecules during the pyrolysis. Further detailed morphology of the $Co(OH)_2$ and $Co_3O_4$ were characterized by TEM (figures 5(C)–(F)). $Co(OH)_2$ is a uniform smooth and intricate wire, shown in the HR-TEM (figure 5(D)), and exhibits crystallinity (inset of figure 5(D)). Its lattice spacing is 0.339 nm in accord with the interspace of the (311) planes. After sintering treatment, the microstructure of $Co_3O_4$ nanowires is further presented by HR-TEM (figures 5(E) and (F)). The individual $Co_3O_4$ nanowires are integrated by a large amount of particles with much interspace between the nanoparticles. Corresponding to the interspace of the (111) planes, the clear high-resolution TEM of the electronic diffraction image demonstrates lattice spacing is 0.469 nm and crystallinity is pretty high.

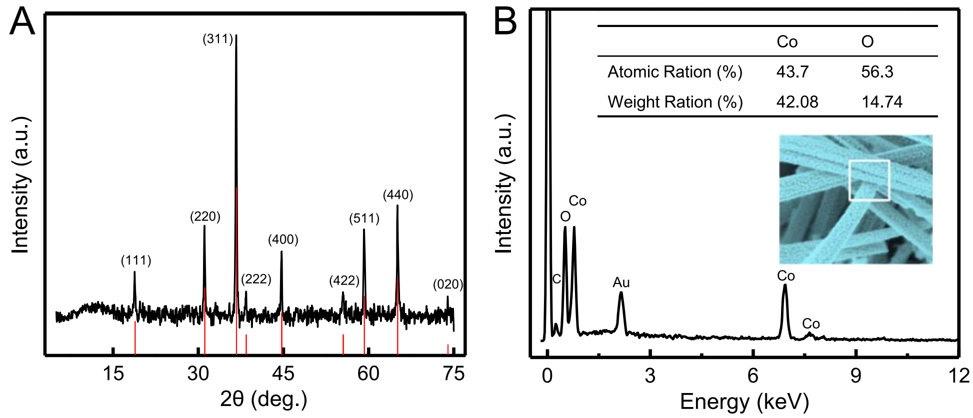

| | Co | O |
|---|---|---|
| Atomic Ration (%) | 43.7 | 56.3 |
| Weight Ration (%) | 42.08 | 14.74 |

**Figure 6.** (A) XRD patterns of $Co_3O_4$ nanowires. (B) The EDX spectrum of $Co_3O_4$ nanowires (inset: selected area for EDX test). The insert table is the ratio of Co and O element.

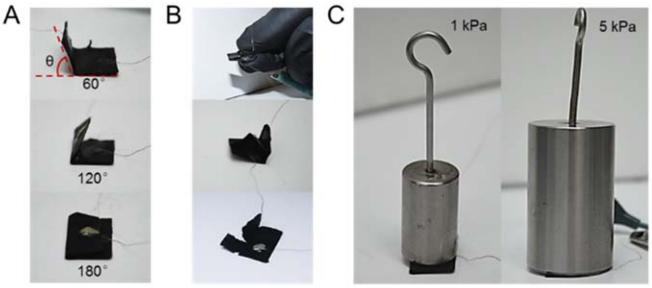

**Figure 7.** Binder-free multi-shapes highly flexible HSs could work in different conditions (A) Different bending models (60°, 120°, and 180°); (B) Giant deformation by hand (top), free giant deformation (middle), and partial breakage of the electrodes; (C) electrodes folded to 180 °and compressed by different stress, 1 kPa (left) and 5 kPa (right), respectively.

Figure 6(A) shows XRD patterns of $Co_3O_4$ nanowires. The $Co_3O_4$ displays nine diffraction peaks which coincide with the standard spectrum of $Co_3O_4$ (PDF#- 09–0418). Figure 6(B) exhibits the EDX spectrum of $Co_3O_4$ nanowire for the selected region (inset). Except for Au peaks (conductive medium) at 2.5 keV, four typical $Co_3O_4$ peaks at 0.52, 0.78, 6.94, and 7.64 keV diffraction patterns are found, which correspond to Co and O elements. The atomic and weight ratios of Co and O are listed in the inserted table with the atomic ratio of 3:4 indicating that the component after sintering treatment is mainly $Co_3O_4$ nanowires.

### 3.5. Device flexibility test applied various external mechanical conditions

The observation of the electrode after depositing $Co_3O_4$ nanowires is shown in figure S3. Figure 7(A) is the device flexibility performance at various bending angles ($\theta$), 60°, 120°, and 180°, where is a pretty small radius of curvature at the folded line. Figure 7(B) shows the as-assembled device could work at diverse harsh external mechanical conditions, such as giant deformation formed by hand (top), free giant deformation (middle), and even partial breakage of the electrodes. In addition, the folded (180°) device could maintain a certain specific capacitance under different stress as shown in figure 7(C) pressed by different amount of weight, such as 20 g (left: 1 kPa) and 100 g (right: 5 kPa). Typically, for the traditional supercapacitor, active electrode material requires to adhere by binding on some frameworks such as nickel mesh and need to package by a metal shell or polymer film. Moreover, for traditional liquid electrolyte supercapacitor, assembled device invariably requires separator film between two electrodes and need a current collector, which results in complicated operation processes for practical application. To simplify the fabrication, the reported HSs in this work are binder free, separator free and all solid state, which is a much more facile strategy to increase the device energy density of the whole supercapacitor weight.

### 3.6. Electrochemical performances of the device in multi-shapes

The flexible annealed CNP/$Co_3O_4$ HSs were executed in solid state electrolyte (KOH/PVA). Figure 8(A) demonstrates the series of CV curves of the flexible HSs within the potential window from −0.8 to 0.8 V and scan rate from 10 to 1000 mv $s^{-1}$. Presenting a good capacitive behavior, the CV curves exhibit nearly

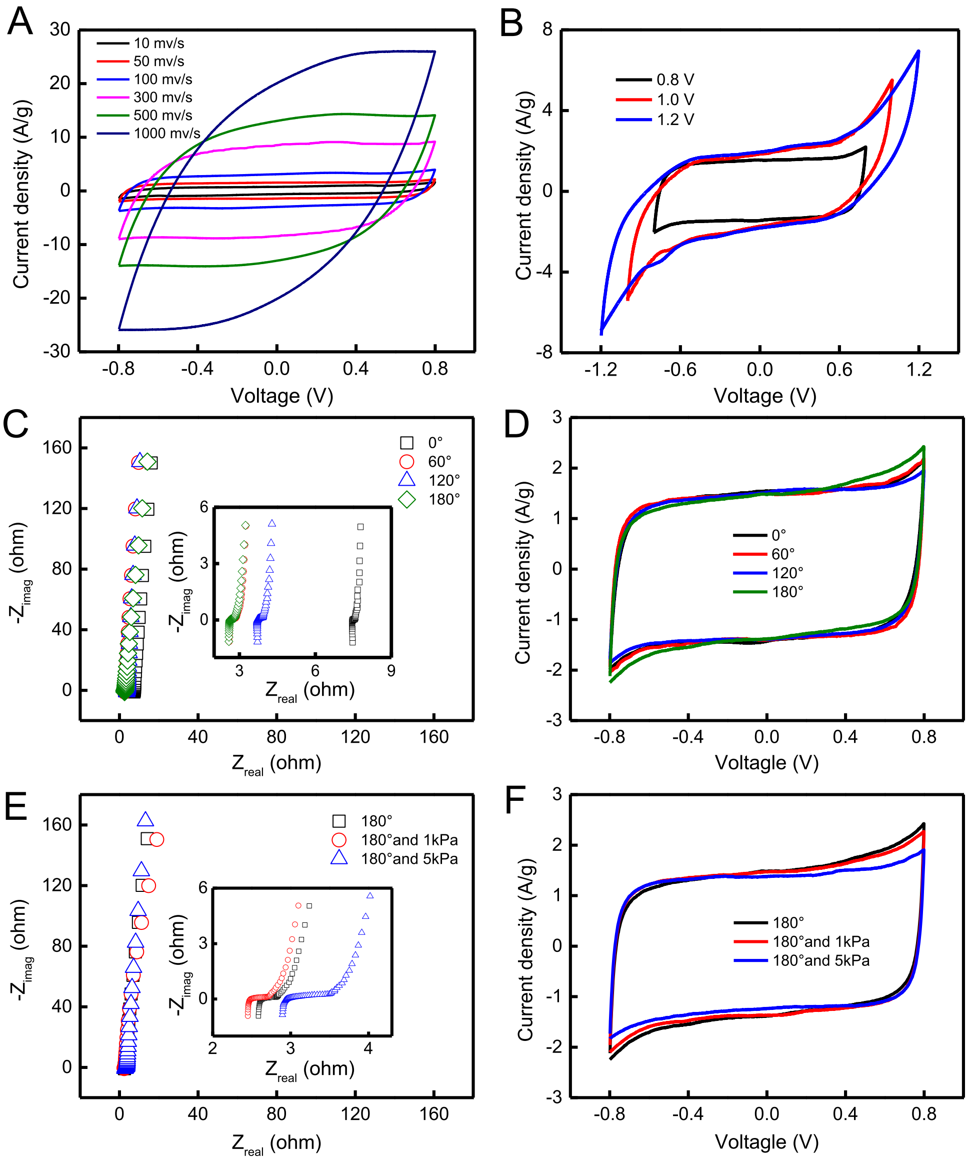

**Figure 8.** (A) CV curves of the annealed CNP/$Co_3O_4$ nanowire HSs at different scan rate from 10 mv $s^{-1}$ to 1000 mv $s^{-1}$. (B) CV curves of different chemical windows at the scan rate of 50 mv $s^{-1}$. Electrochemical performance of the ultra- flexible annealed CNP/$Co_3O_4$ nanowire HSs measured at different harsh mechanical conditions. (C) Nyquist plots of the annealed CNP/$Co_3O_4$ HSs executed at various bending angle from 0 °to 180°. Inset is the enlarged plots at high frequency; (D) The corresponding CV curves in the different bending angles of figure 8(C) at the scan rate of 50 mv $s^{-1}$ (E) Nyquist plots of the hybrid device carried out in 180° bending angle and a certain amount of stress. Inset is the enlarged curves at high frequency. (F) The corresponding CV curves of figure 8(E) at the scan rate of 50 mv $s^{-1}$.

rectangular shapes over a large voltametric currents and wide range of scan rates. When the scan rate was 500 mv $s^{-1}$, the CV curves also retain rectangular shapes with little distortion, showing fast ion diffusion rate from the electrolyte into the electrodes and low equivalent series resistance (ESR). Derived from CV curves, the maximum specific capacitance is about 330.8 F $g^{-1}$ at 10 mv $s^{-1}$ as shown in figure S4(A). However, the specific capacitance decreases to 57.8 F $g^{-1}$, as the scan rate increased to 1000 mv $s^{-1}$ gradually. Figure 8(B) shows CV curves of the highly flexible HSs with different chemical windows from −0.8–0.8 V to −1.2–1.2 V. The presence of weak redox peaks (operating cell voltages at 1.0 and 1.2 V in the region ~0.5 V) indicates that the pseudocapacitive properties of the devices originated from the $Co_3O_4$ nanowires. At the operating potential to 1.2 V, the increasing surrounding area from the corresponding CV curve indicates the Faradic reactions occurred. As described above, the reported HSs are fabricated in a binder free, separator free and current collector free system. To reveal the devices flexibility, the HSs carried out in many harsh external mechanical conditions, such as tiny radius curvature bending, compressing and tearing design.

Figure 8(C) is the Nyquist plots of the hybrid device executed in different small radius curvature (figure 7(A)). As we known, Nyquist curve can be distinguished into two parts. One is the semicircle located in high frequency; the intersection of the real axis and the curve indicates the electrolyte resistance (Rs), which represents the ohmic resistance of the electrolyte and electrodes. At the low frequency region of the semicircle, the intercept of the real axis and the semicircle regard as the contact resistance. The other part of the Nyquist curve located in the low frequency is the Warburg resistance represented by the straight line inclined at 45° with the real axis. From figure 8(C) and the inset image, all the plots form a nearly vertical and straight line in the low frequency, illustrating a nearly ideal capacitive behaviour. The ESR values of different bending angles (from 0° to 180°) are 7.47, 2.59, 3.71, and 2.58 Ω, respectively, which is lower than the previous reports of all solid state supercapacitors [51, 52]. The lower ESR value attribute to the highly conductivity of the annealed CNP for the deposition of $Co_3O_4$ nanowires and low internal resistance of the electrodes. The decrease from 7.47 to ~3 Ω may be caused by the distance decreasing of the anode and cathode resulting in lower electrolyte resistance of bending conditions. The charge transfer resistances are all ~0.3Ω, which manifests the as-prepared devices possess excellent ion interaction behaviour. Figure 8(D) is the corresponding CV curves of the HSs at different bending angles. The surrounding area of the CV curves confirms that no significant degradation was observed during bending at various angles, indicating the capacitive performance was retained after bending. Figure 8(E) is the Nyquist plots of the flexible device carried out at 180° in small radius curvature and weighted a certain amount of stress as illustrated in figure 7(C). From the inset plot, the $x$ axis intercept of Nyquist plots is 2.59 Ω, 2.45 Ω, and 2.89 Ω, respectively for different conditions (from the black square curve to blue triangle curve). It is obvious that the resistance of electrodes and electrolyte has little change after weighting a certain amount of load on folded devices. The low ESR value exhibits the device conductivity could be maintained after the bending and weighting load. In addition, charge transfer resistance is 0.23 Ω, 0.32 Ω, and 0.67 Ω, respectively (from the black square curve to blue triangle curve). As the weighting load increasing, the corresponding charge transfer resistance is raised, which might may be caused by the compact density increase of the $Co_3O_4$ nanowire layer during loading stress leading to the ion diffusion resistance increase. However, the charge transfer is still much lower than the previous reports, due to the highly porous of the annealed CNP and the $Co_3O_4$ nanowire layer (figures 2(C) and S3). Figure 8(F) is the CV corresponding curves of figure 8(E). There was no appreciable difference in different conditions when the HS was folded by 180°and stressed which proves excellent flexibility and stability of the devices. In addition, the surrounding areas of figures 8(D) and 6(F) show that no obvious change was observed, meaning the capacitive performance is maintained in the harsh external mechanical conditions. As far as we known, the applied bending radius of curvature in this paper is the smallest ones than the previous reports. Therefore, based on the above analysis, the as-prepared HSs possess ultra-high flexibility and stability in harsh external mechanical conditions.

As an ultra-flexible device, it should be maintained a certain electrochemical performance at different external mechanical conditions such as bending, compressing, and even tearing. Figure 9(A) is the CV curves of the flexible device executed in different external conditions at 50 mv $s^{-1}$. Obviously, the CV shapes are slight change for the 0°, 180°, and arbitrary shape (AS) revealing the capacitive performance has no obvious degradation during the external mechanical change (corresponding specific capacitance is shown in figure S4(B)). Rectangular shape shows the conductivity of the HSs can be maintained in the various shapes. To investigate the limit flexibility of the device, the device was partially torn as shown in figure 4(B) (bottom). CV test of tearing device is provided in the pink curve. It is recognizable that the shape of the CV curve is moderate round as the other three external conditions meaning the ESR is increasing. The specific capacitance calculated by CV curve at 50 mv $s^{-1}$ for the diverse external conditions is shown in figure S4(B). The specific capacitance for different types is 109.1 F $g^{-1}$, 110.6 F $g^{-1}$, 102.8 F $g^{-1}$, and 88.8 F $g^{-1}$, respectively. Capacitance retention is 81.3% of 0°device for the partially torn (PT) device exploring that the capacitive performance is affected slightly during the external tearing damage. The capacitive performance demonstrates outstanding flexibility, high conductivity of the annealed CNP electrode and the excellent performance of resisting external mechanical conditions. Figure 9(B) is the corresponding Nyquist plots of figure 9(A). One could find that obvious semicircles appeared at the high frequency in the zoom in plot. ESR of the PT device is a little higher than 0 °and 180° bending conditions, which is associated with the CV curves of figure 9(A). From the low frequency segment, the PT device bends to the axis which may be caused by spherical diffusion effect due to the damage of the electrode. For 0° sample, figure 9(C) displays the charge-discharge curves with different current densities. The time of discharge branch excludes IR drop shown in the curve angulus parietalis. No significant IR drop is observed at the beginning of discharge branch at low current density indicating the gentle contact resistance in the device. As shown in the curves, total charge-discharge time decreases along with the increasement of current density. Moreover, the symmetrical and linear profiles at various current densities signifying the excellent capacitive characteristic are performed the charge-discharge curves of the device. The device exhibits the gravimetric capacitance of 343.2 F $g^{-1}$ at the current density of 0.15 A $g^{-1}$, and retains 140.4 F $g^{-1}$ at the current density of 1.5 A $g^{-1}$, which improves greatly than the flexible supercapacitors with carbon nanotubes grown on carbon cloth and activated carbon cloth. As increasing the applied current density, high current density leads to the decrease of specific capacitance (inset of figure 9(C)), which may be caused by low ionic mobility of gel electrolyte. The charge-discharge curve at a 1 A $g^{-1}$ current density described the long-term stability of a 0°

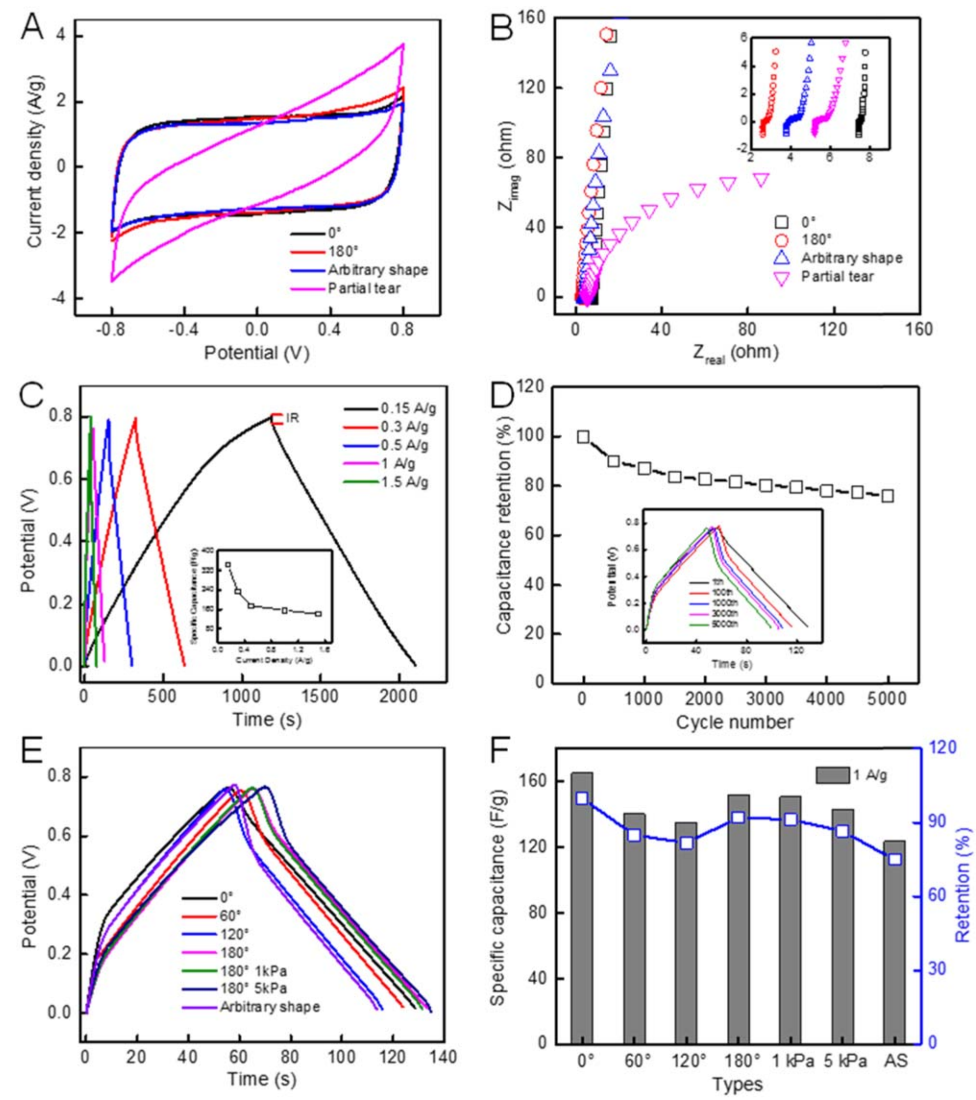

**Figure 9.** (A) CV curves of the hybrid device working in different executed shapes at 50 mv $s^{-1}$. (B) The corresponding Nyquist plots of figure 9(A), inset is the zoom in at high frequency. (C) Charge-discharge curves of a 0 °device performed at different current densities, inset is the specific capacitance curve at the corresponding current densities. All the discharge time is calculated exclude the IR drop as shown in discharge segment at 0.15 A $g^{-1}$. (D) Cycling performance of the flexibility HSs at a current density of 1 A $g^{-1}$ for 5000 cycles, inset is the charge-discharge curves after a certain cycles. (E) Charge-discharge curves at various external mechanical conditions applied on the device at the current density of 1 A $g^{-1}$. (F) Specific capacitance corresponding to the conditions of figure 9(E) and capacitance retention as 0° state.

device (figures 9(D) and S5). The result shows capacitance retention of 75.9% over 5000 cycles signifying a superior stability of the solid state ultra-flexible supercapacitor. To further investigate the capacitive performance at various external conditions, the charge-discharge measurement at the 1 A $g^{-1}$ current density of is found in figure 9(E) for various external conditions. Thus, it is clear that the full discharge time performs no perceptible degradation in all conditions, which indicate good electrochemical performance of the flexible device even under small radius curvature fold and stress load coexistence. Furthermore, figure 9(F) displays the corresponding specific capacitance of figure 9(E). The specific capacitance of AS is 123.8 F $g^{-1}$, which shows capacitance retention of ~75% capacitance of 0 °device (163.8 F $g^{-1}$), illustrating an admirable flexibility and electrochemical performance of the hybrid device to adapt various external conditions.

## 4. Conclusions

This paper has proposed a binder free, current collector free and separator free ultra-flexible solid state HSs based on thermo-crosslinking CNP and $Co_3O_4$ nanowires via a facile strategy. The thermo-crosslinking CNP was obtained by high temperature annealing to improve mechanical property and flexibility of the as-prepared CNP. Benefiting from annealed CNP, the as-prepared device could be executed in various external conditions, such as bending, compressing and tearing design, and displays high capacitive performance that is 330.8 F $g^{-1}$ at scan rate of 5 mv $s^{-1}$ and 345.8 F $g^{-1}$ at current density of 0.15 A $g^{-1}$. The retention capacitance in different external conditions is 74.9%–81.3%. Long-term stabile testing shows the hybrid device retained about ~75.9% of the intimal capacitance after 5000 cycles. The results indicate the paper provides a feasible strategy for resisting harsh external mechanical behaviours to guarantee safety of the power supply system. The proof-of-concept is necessary for future supercapacitor dependent application field and open up a novel pathway to achieve ultra-flexible, lightweight, high performance supercapacitor electrode substrate by high temperature annealing.

## Acknowledgments

This work is supported by the National Natural Science Foundation of China (Grant No. 11632005, 11672086). Project supported by the Foundation for Innovative Research Groups of the National Natural Science Foundation of China [Grant No. 11421091].

## ORCID iDs

Yanju Liu https://orcid.org/0000-0001-8269-1594
Jinsong Leng https://orcid.org/0000-0001-5098-9871

## References

[1] Xiong Z, Liao C, Han W and Wang X 2015 *Advanced Materials* **27** 4469
[2] Zhao Y, Meng Y and Peng J 2014 *Journal of Power Sources* **259** 219
[3] Wang K, Zhang X, Li C, Sun X, Meng Q, Ma Y and Wei Z 2015 *Advanced Materials* **45** 7451–57
[4] Chen T, Hao R, Peng H and Dai L 2015 *Angewandte Chemie International Edition* **127** 628
[5] Son D, Lee J, Qiao S, Ghaffari R, Kim J, Ji E L, Song C, Kim S J, Dong J L and Jun S W 2014 *Nature Nanotechnology* **9** 397
[6] Guo W, Xu C, Zhu G, Pan C, Lin C and Wang Z L 2012 *Nano Energy* **1** 176
[7] Park S and Jayaraman S 2003 *MRS Bulletin* **28** 585
[8] Wang K, Wu H, Meng Y and Wei Z 2014 *Small* **10** 14
[9] Cherusseri J and Kar K K 2015 *Journal of Materials Chemistry A* **3** 21586
[10] Zhou G, Li F and Cheng H M 2014 *Energy & Environmental Science* **7** 1307
[11] Wang G, Babaahmadi V, He N, Liu Y, Pan Q, Montazer M and Gao W 2017 *Journal of Power Sources* **367** 34
[12] Pan Q, Shim E, Pourdeyhimi B and Gao W 2017 *Langmuir* **33** 7452
[13] Pan Q, Shim E, Pourdeyhimi B and Gao W 2017 *ACS applied materials & interfaces* **9** 8308
[14] Zeng S, Chen H, Cai F, Kang Y, Chen M and Li Q 2015 *Journal of Materials Chemistry A* **3** 23864
[15] Chen Y, Du L, Yang P, Sun P, Yu X and Mai W 2015 *Journal of Power Sources* **287** 68
[16] Horng Y Y, Lu Y C, Hsu Y K, Chen C C, Chen L C and Chen K H 2010 *Journal of Power Sources* **195** 4418
[17] Pan Q, Tong N, He N, Liu Y, Shim E, Pourdeyhimi B and Gao W 2018 *ACS applied materials & interfaces* **10** 7927
[18] Lu X, Yu M, Wang G, Tong Y and Li Y 2014 *Energy & Environmental Science* **7** 2160
[19] Lu X, Dou H, Yuan C, Yang S, Hao L, Zhang F, Shen L, Zhang L and Zhang X 2012 *Journal of Power Sources* **197** 319
[20] Liu F, Han G, Chang Y, Fu D, Li Y and Li M 2014 *Journal of Applied Polymer Science* **131** 39779
[21] Ghaffari M, Kosolwattana S, Zhou Y, Lachman N, Lin M, Bhattacharya D, Gleason K K, Wardle B L and Zhang Q M 2013 *Electrochimica Acta* **112** 522
[22] Wang Y, Chen J, Cao J, Liu Y, Zhou Y, Ouyang J H and Jia D 2014 *Journal of Power Sources* **271** 269
[23] Cui X, Lv R, Sagar R U R, Liu C and Zhang Z 2015 *Electrochimica Acta* **169** 342
[24] Ghoniem E, Mori S and Abdel-Moniem A 2016 *Journal of Power Sources* **324** 272
[25] Jin F D, Yong R K and Jeong H T 2016 *Chemistry Select* **1** 1–11
[26] Chen Y, Gao Z, Zhang B, Zhao S and Qin Y 2016 *Journal of Power Sources* **315** 254
[27] Roberts M E, Wheeler D R, Mckenzie B B and Bunker B C 2009 *Journal of Materials Chemistry* **19** 6977
[28] Sun L, Wang X, Zhang K, Zou J and Zhang Q 2016 *Nano Energy* **22** 11
[29] Liu Y, Weng B, Razal J M, Xu Q, Chen Z, Hou Y, Seyedin S, Jalili R, Wallace G G and Chen J 2015 *Scientific Reports* **5** 17045
[30] Chabi S, Peng C, Yang Z, Xia Y and Zhu Y 2015 *RSC Advances* **5** 3999
[31] Jiang S, Shi T, Zhan X, Long H, Xi S, Hu H and Tang Z 2014 *Journal of Power Sources* **272** 16
[32] Xu J, Wang Q, Wang X, Xiang Q, Liang B, Chen D and Shen G 2013 *Acs Nano* **7** 5453
[33] Ren X, Guo C, Xu L, Li T, Hou L and Wei Y 2015 *Acs Applied Materials & Interfaces* **7** 19930
[34] Naoi K, Kurita T, Abe M, Furuhashi T, Abe Y, Okazaki K, Miyamoto J, Iwama E, Aoyagi S and Naoi W 2016 *Advanced Materials* **28** 6751
[35] Hu C, Xu H, Liu X, Zou F, Qie L, Huang Y and Hu X 2015 *Scientific Reports* **5** 16012
[36] Guo C X, Yilmaz G, Chen S, Chen S and Lu X 2015 *Nano Energy* **12** 76
[37] Zhang Z, Xiao F, Qian L, Xiao J, Wang S and Liu Y 2014 *Advanced Energy Materials* **4** 867
[38] Bao L, Zang J and Li X 2011 *Nano Letters* **11** 1215
[39] Meng C, Liu C and Fan S 2009 *Electrochemistry Communications* **11** 186
[40] He S, Wei J, Guo F, Xu R, Li C, Cui X, Zhu H, Wang K and Wu D 2014 *Journal of Materials Chemistry A* **2** 5898
[41] Che J, Chen P and Chanpark M 2013 *J. Mater. Chem. A* **1** 4057
[42] Cheng C E, Lin Y C, Tsai S Y, Lin Z K, Lee P C, Miao H Y, Chang C S and Chien S S 2015 *Journal of Physics D Applied Physics* **48** 355107
[43] Yang X, Lee J, Yuan L, Chae S R, Peterson V K, Minett A I, Yin Y and Harris A T 2013 *Carbon* **59** 160
[44] Chu H, Zhang Z, Liu Y and Leng J 2014 *Carbon* **66** 154
[45] Chu H, Zhang Z, Liu Y and Leng J 2016 *Carbon* **98** 557

[46] Zhou C and Liu J 2014 *Nanotechnology* **25** 035402
[47] Jian Z, Wei Z, Liu X, Chen A, Liu Z and Huang F 2014 *Advanced Functional Materials* **24** 2013
[48] Zhang X, Jiang K, Feng C, Liu P, Zhang L, Kong J, Zhang T, Li Q and Fan S 2006 *Advanced Materials* **18** 1505
[49] Goggin P R 1963 *Nature* **199** 367
[50] Filleter T and Espinosa H D 2013 *Carbon* **56** 1
[51] Liu Y, Weng B, Razal J M, Xu Q, Zhao C, Hou Y, Seyedin S, Jalili R, Wallace G G and Chen J 2015 *Scientific Reports* **5** 17045
[52] Xiao F, Yang S, Zhang Z, Liu H, Xiao J, Wan L, Luo J, Wang S and Liu Y 2015 *Scientific Reports* **5** 09359